AIAA 03–3963

Inflow Boundary Conditions for Compressible Turbulent Boundary Layers

Sheng Xu and M. Pino Martin
Department of Mechanical and Aerospace Engineering
Princeton University, Princeton, NJ

16th AIAA Computational Fluid Dynamics Meeting and Exhibit
June 22–26, 2003/Orlando, FL

Inflow Boundary Conditions for Compressible Turbulent Boundary Layers

Sheng Xu and M. Pino Martin
Department of Mechanical and Aerospace Engineering
Princeton University, Princeton, NJ

We analyze, from the energy perspective, why the use of genuine periodic boundary conditions, in which no alteration of governing equations is made, results in growing mean flow and decaying turbulence in simulations of turbulent boundary layers. The premises under which the usage is valid are presented and explained. The extended temporal approach[1] is addressed. It is used to assess the validity of the use of genuine periodic boundary conditions. Extending the work by Lund *et al.*,[2] we propose an inflow generation method for spatial simulations of compressible turbulent boundary layers. The method assumes that the compressibility effects reduce to density variation effects and that general temperature-velocity relationships exist in the boundary layers. It generates inflow by reintroducing to an inlet the rescaled downstream flow field. Test results indicate that it is an efficient and accurate method.

Introduction

The simulation of a turbulent boundary layer requires streamwise inflow and outflow boundary conditions. The use of a buffer domain[3] or a sponge layer[4,5] in combination with non-reflecting boundary conditions can successfully handle the outflow. The specification of the inflow boundary conditions, however, is more problematic and challenging. A turbulence eddy in a boundary layer has the memory of its upstream history. This fact makes it desirable to specify a realistic time series of turbulence at the simulation inlet. A method to generate a time series of turbulence data usually has conflict between efficiency and accuracy. To create accurate inflow may require detailed independent simulations and can be costly. While a cost-saving but crude inflow generation method needs a long development section behind the inlet for a flow to evolve to be realistic. Typical inflow generation techniques can be organized into three categories, as shown in Fig. 1.

The first category consists of the fringe method,[6] the rescaling method[2,7] and methods for temporal simulation.[1,8,9] The inflow in this category comes from the outflow with or without modification. The fringe method distinguishes a fringe region, in which finite extra terms are added to the governing equations to remove mass and decrease boundary layer thickness, and a useful region for data collection, in which there are no extra terms. In the streamwise direction, the simulation domain is assembled with one useful region and two fringes at its ends and periodic boundary conditions are applied. Thus, the flow that goes out from the downstream end of the data collection region comes into the upstream end after passing through the two fringes. The method results in a spatial simulation and can take into account the streamwise pressure gradient. The rescaling method is based on scaling laws of turbulent boundary layers. The inflow is generated by rescaling the velocity field at a downstream station and reintroducing it at the upstream inlet. It can be easily implemented to yield a spatial simulation and works very well with little or no transient near the inlet boundary, thought there are potential enhancements that may serve to increase its utility futher. In temporal simulations, periodic boundary conditions are used, artificially making the inflow exactly the same as the outflow. A turbulence eddy going out from the outlet comes back into the domain at the inlet without any modifications. To reduce artificial effects, the streamwise size of the domain should be large enough at least to decorrelate turbulence eddies at the inlet and those in the middle between the inlet and the outlet. A genuine temporal simulation solves the original governing equations, while improved temporal simulations adds forcing in the governing equations to account for the streamwise inhomogeneity of boundary layers.

The second category involves inflow generation by outside mechanisms, such as an auxiliary simulation and superposition of random fluctuations on desired mean profiles. Li *et al.*[10] present a method to generate the inflow boundary conditions for large eddy simulations (LES) of turbulent free shear flows. In the method, a time series of instantaneous velocity planes from an auxiliary simulation is recycled repeatedly to provide the inflow. They transform the time signal into a periodic one using a windowing technique. The periodicity induced by the inflow takes 25% of their test domain to die out. Adams[11] used a similar approach to provide the inflow for his direct numerical simulation

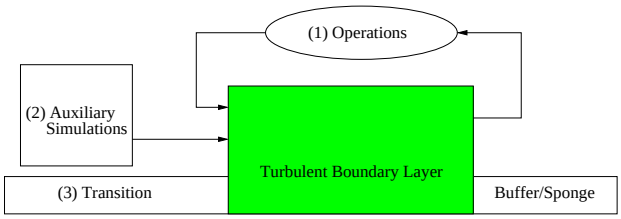

Fig. 1 Schematic showing inflow generation techniques.

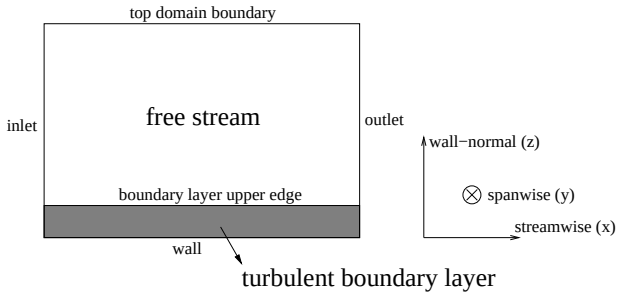

Fig. 2 Schematic of the control volume for analysis in TDNS.

(DNS) of a turbulent compression ramp. Large-Eddy Simulation (LES) of supersonic compression-ramps by Rizzeta *et al.*[12,13] and DNS of turbulent flow over a rectangular trailing edge by Yao *et al.*[14] also use auxiliary simulations to generate turbulence inflow. The specification of the inflow by superposition of random fluctuations on mean flows is a straightforward procedure. This procedure is successful in the simulations of spatially decaying compressible isotropic turbulence.[15] Other implementations with varying degrees of success include DNS of the spatial laminar-to-turbulent transition[16] and DNS of a backward-facing step.[17] The shortcoming of the method is the requirement of a fairly long development section due to the lack of proper phase information and nonlinear energy transfer. Also, it is very hard to control the skin friction and integral thickness at the end of the development section. Klein *et al.*[18] develop a method for generating pseudo turbulent inflow. It provides some advantages over the classical approach that uses random fluctuations. The method is based on digital filtering of random data and is able to reproduce a prescribed one-point second order statistics as well as autocorrelation functions.

The last category has the most straightforward approach.[16,19] The computation of the spatially developing turbulent boundary layer starts far upstream, where a laminar profile plus disturbances is set up to allow a transition to turbulence. No time-dependent inflow is required, but the cost is daunting. The approach is generally used to investigate transition itself, see Ref. 20–23.

In the current paper, we first discuss and analyze the use of periodic boundary conditions toward temporal simulations. We introduce the genuine temporal direct numerical simulation (TDNS) and an extended temporal direct numerical simulation (ETDNS). We then present a rescaling method for spatial simulation of compressible turbulent boundary layers. Test comparisons between TDNS and ETDNS are made. Results from the rescaling method are given and also compared with those from the marching process of ETDNS.

Periodic boundary conditions

Periodic boundary conditions are widely used in homogeneous directions in turbulent simulations. The usage is proved to be valid by many numerical experiments, though it may not be well justified physically. The advantages of periodic boundary conditions are apparent. No external inputs are required, Fourier representation is applicable and statistical samples are improved. However, their homogeneity requirement usually limits them to simple geometries, such as rectangular isotropic turbulence boxes, turbulent plane channels and turbulent pipes.

A flat-plate boundary layer under zero-pressure gradient evolves slowly in the streamwise direction and lacks streamwise homogeneity. If the effect of the streamwise inhomogeneity is neglected, periodic boundary conditions may be applied, leading to a temporal behavior of the boundary layer. The majority of boundary layer transition simulations used temporal approaches and achieved notable success accompanied with limitations, see Ref. 24. In turbulent boundary layer simulations, streamwise periodicity may still be assumed, as addressed in the following two sections for DNS.

TDNS

The use of genuine periodic boundary conditions in DNS of a zero-pressure-gradient turbulent boundary layer is to apply them in the streamwise direction, besides the span wise direction, without any change to the governing equations. As a result, the simulation is temporal instead of spatial and we call it temporal DNS (TDNS). In TDNS, non-stationary statistics are obtained, that is the mean streamwise velocity profile develops in time and the turbulence decays in time. Also, the wall-normal displacement in the free stream is prohibited. We can verify these aftereffects from the mathematical description of the simulated problem.

Taking the simulation domain as a control volume $\mathcal{V}$ and denoting its surface as $\mathcal{S}$, as shown in Fig. 2, we integrate the continuity equation and have the following

$$\frac{\partial}{\partial t}\int_{\mathcal{V}} \rho \mathrm{d}\mathcal{V} + \oint_{\mathcal{S}} \rho u_j n_j \mathrm{d}\mathcal{S} = 0, \tag{1}$$

where n_j is the normal vector of the surface $\mathcal{S}$. Starting from the continuity and momentum equations, we

can deduce the equation for total kinetic energy K ($= \frac{1}{2}\rho u_i u_i$) as

$$\frac{\partial K}{\partial t} + \frac{\partial u_j K}{\partial x_j} = \frac{\partial u_i \sigma_{ij}}{\partial x_j} + pS_{kk} - \Phi, \tag{2}$$

where σ_{ij} is the stress tensor and Φ is the dissipation given by

$$\begin{aligned} \sigma_{ij} &= -p\delta_{ij} + \tau_{ij} \\ &= -p\delta_{ij} + 2\mu\left(S_{ij} - \frac{1}{3}S_{kk}\delta_{ij}\right), \qquad (3) \\ \Phi &= 2\mu\left(S_{ij}S_{ij} - \frac{1}{3}S_{kk}^2\right), \qquad (4) \end{aligned}$$

where τ_{ij} is the shear stress tensor, $S_{ij} = \frac{1}{2}\left(\frac{\partial u_i}{\partial x_j} + \frac{\partial u_j}{\partial x_i}\right)$ is the strain tensor and μ is the dynamic viscosity. Integrating Eq. (2) over $\mathcal{V}$ results in

$$\begin{aligned} \frac{\partial}{\partial t}\int_{\mathcal{V}} K \mathrm{d}\mathcal{V} + \oint_{\mathcal{S}} (u_j K - u_i\sigma_{ij}) n_j \mathrm{d}\mathcal{S} \\ = \int_{\mathcal{V}} pS_{kk}\mathrm{d}\mathcal{V} - \int_{\mathcal{V}} \Phi \mathrm{d}\mathcal{V}, \end{aligned} \tag{5}$$

With symmetric boundary conditions at the top boundary of the domain, no-slip and no-penetration boundary conditions at the wall and periodic boundary conditions in the streamwise and spanwise directions, no wall-normal displacement at the top boundary follows Eq. (1) to conserve mass in the domain, and the second term in Eq. (5) thus vanishes. In an incompressible case, the pressure dilatation, the third term in Eq. (5), is zero while the dissipation is always greater than zero, the total kinetic energy in the domain therefore always decrease with time. This is also apparent from an energy conversion and conservation point of view.

According to Eq. (5), the free stream outside the boundary layer supplies energy to the flow within the boundary layer through convection and work by shear and pressure. Turbulence is mainly confined within the boundary layer and is sustained by the mean flow energy. For an incompressible turbulent boundary layer with the same boundary conditions as above, the integral equations resembling Eq. (5) for the mean and turbulent kinetic energy are respectively

$$\frac{\partial}{\partial t}\int_{\mathcal{V}} K_m \mathrm{d}\mathcal{V} = -\int_{\mathcal{V}} \mathcal{P}\mathrm{d}\mathcal{V} - \int_{\mathcal{V}} \Phi_m \mathrm{d}\mathcal{V}, \tag{6}$$

$$\frac{\partial}{\partial t}\int_{\mathcal{V}} K_t \mathrm{d}\mathcal{V} = \int_{\mathcal{V}} \mathcal{P}\mathrm{d}\mathcal{V} - \int_{\mathcal{V}} \Phi_t \mathrm{d}\mathcal{V}, \tag{7}$$

where $K_m = \frac{1}{2}\rho\langle u_i\rangle\langle u_i\rangle$ is the mean kinetic energy, $K_t = \frac{1}{2}\rho\langle u_i' u_i'\rangle$ is the turbulent kinetic energy, $\mathcal{P}$ is turbulence production, Φ_m and Φ_t are mean and turbulence dissipation respectively. We use $\langle\cdot\rangle$ to denote a spatial average in a homogeneous plane and a prime the fluctuation with respect to a spatial mean. $\mathcal{P}$, Φ_m and Φ_t are all non-negative within the boundary layer. So the mean kinetic energy within the boundary layer decays and the mean streamwise velocity profile develops in time, which results in the thickening of the boundary layer. The mean flow evolution also leads to a decrease in the turbulence production and causes the decay of the turbulence.

The pressure dilatation in Eq. (5) represents a transfer mechanism between internal energy and kinetic energy other than dissipation. In a compressible case, similar terms appear in the integral equations corresponding to Eq. (6) and Eq. (7), but they are not dominant in the energy balances if the turbulent Mach number is not very high. In a supersonic turbulent boundary layer, the pressure dilatation in the turbulent kinetic energy balance is negative in the wall vicinity, resulting in a transfer of kinetic to internal energy, and assumes small positive values approaching zero away from the wall. So we can extrapolate the above analysis and arguments for an incompressible case to a supersonic case.

In summary, the use of genuine periodic boundary conditions in DNS of a zero-pressure-gradient turbulent boundary layer results in a temporal DNS (TDNS). Taylor's frozen turbulence hypothesis has been found to be valid if the viscous forces are negligible, the mean shear is small and the turbulence level is low, see Ref. 25. It may be used to relate a spatial simulation and a temporal one through a Galilean transformation with a convective velocity, which can be defined through spectra or space-time correlation functions. Lee *et al.*[15] investigated the applicability of Taylor's hypothesis in spatially decaying compressible isotropic turbulence. They found good match between their spatial and temporal simulations when the turbulence intensity and the fluctuation Mach number are low. The convection velocity was found to be equal to the free stream velocity. But when the turbulence Mach number is high, compressibility-driven quantities in the temporal simulation differ from the spatial one. Fluctuations in the form of acoustic waves propagate in all directions with the local sound speed, which ruins the use of Taylor's hypothesis in compressibility-dominated statistics. So the bridges connecting temporal and spatial simulations through Taylor's hypothesis for supersonic and hypersonic turbulent boundary layers are broken due to their high compressibility, high turbulence intensities, large mean shear and large viscous effects. Nevertheless, TDNS with periodic boundary conditions may still be used to simulate these flows at a particular streamwise location. The necessary conditions are that (i) the turbulence can be considered quasi-steady, i.e. it adjusts itself to local conditions much faster than the mean profile develops; and (ii) for the purpose of gathering

Fig. 3 Schematic of the domains for ETDNS.

statistics, the sampling time is shorter than the time scale of the mean profile development. A flow that satisfies these conditions evolves slowly and can be viewed as a good approximation of a stationary station of a boundary layer.

The necessity of the second condition is apparent. Otherwise, correct statistics are inhibited as the mean flow changes apparently in a non-self-similar way. The first condition ensures the second one. It is necessary to initialize the flow field to nearly equilibrium for realization of these conditions. If the initial flow field is far away from equilibrium, TDNS may require a long temporal transient process before it settles down to a quasi-stationary status. Thus, we could hardly control the skin friction and the boundary thickness at the end of the transient. Martin[26] address the procedure for the initialization of compressible turbulence at nearly equilibrium conditions.

ETDNS

The streamwise periodicity in TDNS leads to a parallel non-stationary mean flow and decaying turbulence due to the neglect of the non-parallel effects of streamwise advection and diffusion in a turbulent boundary layer. These effects can be recovered through the addition of forcing to the basic equations.

Realizing the fact that both the boundary layer thickness and the energy level of the turbulence vary slowly as functions of the streamwise location, Spalart *et al.*[8,9] introduced a new wall-normal coordinate and then applied a multiple-scale procedure to approximate the slow streamwise growth of the boundary layer. The final product is a set of small forcing terms that are added to the Navier-Stokes equations. They used the technique and successfully simulated an incompressible turbulent boundary layer at four streamwise stations. Guarini *et al.*[27] extended the technique to compressible turbulent boundary layer simulations.

Maeder *et al*[1] further developed the procedure by Spalart *et al.*,[8,9] and proposed an extended temporal DNS (ETDNS) approach in which no *a priori* assumptions about the mean flow are required. The ETDNS computes a flow at a series of streamwise stations, as seen in Fig. 3, allowing the spatial mean flow evolution to be approximated from its upstream history. When a sufficiently stationary state is reached at a station, the computational box can be marched downstream another spatial step. In ETDNS, the forcing is derived from the spatial evolution history of the mean flow such that the parabolized Navier-Stokes equations are recovered, which is solved locally in time by DNS. Both the mean flow non-parallelism and the interaction of mean flow non-parallelism with local fluctuations are accounted for in the forcing. For the mathematical derivation of the forcing, we refer to Ref. 1.

There are two remarks worth mentioning for the implementation of ETDNS. One is about the geometric set-up of a simulation and the other regards the forcing at the first station where no upstream history exists, see Fig. 3. The streamwise extent of the domain should be small enough to ensure modest mean flow variation while long enough for turbulence to be decorrelated as in TDNS. In contrast to the simulation by Maeder *et al.*,[1] our simulation presented later relaxes the former to satisfy the latter. The distance between neighboring stations also has contradictory requirements. It should be long enough to avoid overlap of stations but short enough to achieve the accuracy of the forcing calculation. At the first few stations, the information about the mean flow development from previous stations is either missing or inaccurate, causing a non-physical spatial transient. We have the same experience as Maeder *et al.*[1] that, in the spatial transient phase, the solution can be marched downstream after the temporal transient has settled down appreciably, even before a stationary state is reached.

The advantages of ETDNS are (i) ETDNS achieves stationary flow behaviors, i.e. the mean profile keeps and the turbulence sustains; (ii) the marching process allows ETDNS to simulate a series of streamwise stations of a spatially developing boundary layer; and (iii) ETDNS requires no *a priori* assumptions about the mean flow. But, like TDNS and the approach by Spalart *et al.*,[8,9] ETDNS is a temporal technique in nature and a turbulent eddy does not march from one station to another.

Rescaling methods

Temporal approaches, such as TDNS and ETDNS, are efficient and useful in turbulent boundary layer simulations, but they intrinsically have both physical and numerical limitations. Many simulations resort to spatial approaches. For example, to numerically investigate the shockwave/turbulent-boundary-layer interaction over a compression ramp, an inflow-outflow spatial simulation can not be evaded. Still, good inflow generation techniques are desired for this kind of spatial simulations. An auxiliary temporal simulation can be used as an inflow generation device,[2,10,11] but there are issues of computational cost, inflow time periodicity and inflow characteristics control. An efficient and accurate way to integrate the inflow generation and the main spatial simulation is highly desirable.

Based on scaling laws of incompressible turbulent boundary layers, Lund *et al.*[2] proposed a rescaling method to generate turbulent inflow for simulations of spatially developing incompressible boundary layers. The method rescales the velocity field at a downstream

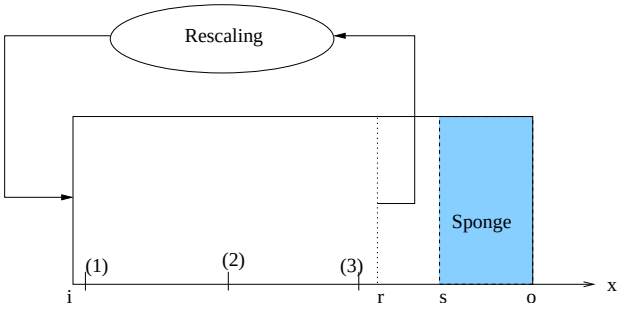

Fig. 4 Schematic of the rescaling methodology.

station and then recycles the rescaled velocity field to the inlet, see Fig. 4. A compressible extension of the method is developed by Urbin *et al.*[7] and is used to simulate a supersonic boundary layer[7] and shock/boundary-layer interaction.[28] The difficulties in the compressible case are that three extra thermodynamic variables, i.e. temperature, density and pressure, need to be rescaled and the velocity field and the temperature field are coupled. Urbin *et al.*[7] treat the temperature in the same way as they rescale the streamwise velocity. The treatment may work numerically for a zero-pressure-gradient boundary layer when the recycling station is close to the inlet. Thus, its applicability is limited. We follow the idea of Lund *et al.*[2] and extend the method to the compressible case. We overcome the difficulties by assuming Morkovin's hypothesis and temperature-velocity relationships. The assumptions are well justified both theoretically and experimentally.

Essentially, Morkovin's hypothesis states that the turbulent time scale in a boundary layer is independent of Mach number. Thus, the effects of Mach number are passive to the dynamics of the turbulent boundary layer, and only affect the variation of the fluid properties. The validity of Morkovin's hypothesis is the reason why van Driest's mean-flow scaling is successful. Following Morkovin's scaling, we rescale the velocity field taking into account the density variation across the boundary layer by using the ratio of local density to wall density ($\frac{\bar{\rho}}{\bar{\rho}_w}$, with an overbar denoting averaging in time and w indicating a wall quantity). In a zero-pressure-gradient boundary layer, the mean pressure is constant and the state equation for perfect gas indicates the mean density variation is equivalent to the mean temperature variation, so the temperature and the velocity are coupled in the rescaling procedure. We therefore need a relation between the mean temperature and the mean velocity for the velocity scaling. Walz's equation (also called modified Crocco relation) is a good approximation for the velocity-temperature relation within a boundary layer under zero pressure gradient, see Ref. 29. To rescale the temperature fluctuations, we also need relationships between the temperature fluctuations and the velocity fluctuations, including amplitude and phase relations. In this regard, we can use the Strong Reynolds Analogy (SRA).

The simulations by Guarini *et al.*[27] and Maeder *et al.*[1] do not support the SRA at Mach numbers as low as 2.5 and 3. In our rescaling method, we only assume that there is some kind of relationship between the temperature and the velocity for the simulated boundary layer, and we do not assume any particular forms of the relationship. Thus, we do not use Walz's equation and the rigorous SRA, as we see below. In this sense, the method presented here is more general.

Due to the presence of multiple length scales in a turbulent boundary layer, we must treat the rescaling process in a piecemeal fashion. To rescale the mean streamwise velocity, we follow Ref. 29 and distinguish the viscous sublayer, the logarithmic region and the law-of-the-wake region in the boundary layer. To rescale the mean wall-normal velocity and turbulence, we divide the boundary layer into the inner layer and outer layer. Hereafter, we denote the streamwise, spanwise and wall-normal coordinates as x,y,z respectively, with the corresponding velocity components as $u(= U + u')$, $v(= V + v')$ and $w(= W + w')$, where a capital letter represents a mean and a lowercase letter with prime represents a fluctuation. We denote the recycled downstream station as $(\cdot)_r$ and the inlet $(\cdot)_i$.

Mean rescaling

For a flat-plate boundary layer, the mean spanwise velocity V is zero due to the spanwise statistical symmetry, and the mean pressure P is equal to the free stream value. Thus, the remaining mean variables to be rescaled are the mean streamwise velocity U, the mean wall-normal velocity W, the mean temperature T and the mean density $\bar{\rho}$.

Mean streamwise velocity

In the viscous sublayer, the viscous shear stress is much larger than the Reynolds shear stress and is assumed equal to the skin friction. Taking the effect of the temperature-dependence of the viscosity, we have

$$\frac{U^s}{u_\tau} = z^+, \tag{8}$$

where $u_\tau = \sqrt{\left(\nu \frac{\partial U}{\partial z}\right)_w}$ is the friction velocity, $z^+ = \frac{u_\tau z}{\nu_w}$ is the wall-normal coordinate in viscous length unit, and U^s is the transformed mean streamwise velocity in the sublayer defined by

$$U^s = \int_0^U \left(\frac{T}{T_w}\right)^n \mathrm{d}U, \tag{9}$$

in which T is the mean temperature and the variation of the viscosity with temperature is given by a power law

$$\frac{\mu}{\mu_w} = \left(\frac{T}{T_w}\right)^n. \tag{10}$$

When $(z^+)_r = (z^+)_i$, i.e.

$$(z)_r = \frac{(u_\tau)_i}{(u_\tau)_r}\frac{(\nu_w)_r}{(\nu_w)_i}(z)_i = \frac{\omega_{u_\tau}}{\omega_\nu}(z)_i, \tag{11}$$

in which

$$\omega_{u_\tau} = \frac{(u_\tau)_i}{(u_\tau)_r}, \quad \omega_{\nu_w} = \frac{(\nu_w)_i}{(\nu_w)_r}, \tag{12}$$

we can compute the transformed velocity U^s at the inlet from

$$(U^s)_i = \omega_{u_\tau}(U^s)_r. \tag{13}$$

In the logarithmic region (also called inertial sublayer), the distance z is assumed to be the only relevant length scale. It can be taken as the mixing length in Prandtl's mixing length theory after multiplying a constant k. A logarithmic law is obtained by using either Prandtl's mixing length theory or just a scale analysis. The effect of density variation is embodied in the velocity scale. The logarithmic law reads

$$\frac{U^{**}}{u_\tau} = \frac{1}{k}\ln z^+ + C, \tag{14}$$

where C is a constant, U^{**} is the van Driest transformed velocity which is defined by

$$U^{**} = \int_0^U \sqrt{\frac{T_w}{T}}\mathrm{d}U. \tag{15}$$

In our scaling method for inflow generation, the above form of the law in the logarithmic region is not needed. We only need to use the following self-similar expression.

$$\frac{U^{**}}{u_\tau} = f_{\log}(z^+), \tag{16}$$

where $f_{\log}$ is assumed to be a universal function, see Ref. 30. So when $(z^+)_r = (z^+)_i$, we have

$$(U^{**})_i = \omega_{u_\tau}(U^{**})_r. \tag{17}$$

In the outer layer of a compressible boundary layer, the different similarity law

$$\frac{U_e^{**} - U^{**}}{u_\tau} = f_{\text{wake}}(\eta), \quad \eta = \frac{z}{\Delta}, \tag{18}$$

applies, where f_{wake} is assumed to be independent of streamwise location x, U_e is the free stream velocity and Δ is an integral reference length taken to be the momentum thickness θ in our rescaling. As the expression indicates, the law is named as the velocity-defect law or the law-of-the-wake. It is well supported by a large number of experiments in zero-pressure-gradient boundary layers. From scaling scheme (18), we can obtain

$$(U^*)_i = \omega_{u_\tau}(U^*)_r,$$
$$U^* = U_e^{**} - U^{**} = \int_U^{U_e} \sqrt{\frac{T_w}{T}}\mathrm{d}U, \tag{19}$$

when $(\eta)_r = (\eta)_i$, i.e. $(z)_r = \frac{(z)_i}{\omega_\Delta}$, where $\omega_\Delta = \frac{(\Delta)_i}{(\Delta)_r}$.

Mean wall-normal velocity

From the mean continuity equation, we can approximate W as

$$W = -\frac{1}{\bar\rho}\int_0^z \frac{\partial \bar\rho U}{\partial x}\mathrm{d}z. \tag{20}$$

We estimate the order of $\frac{\partial \bar\rho U}{\partial x}$ to be $\frac{\bar\rho}{x}\sqrt{\frac{\bar\rho_w}{\bar\rho}}u_\tau$. The order of W then is $\frac{z}{x}\sqrt{\frac{\bar\rho_w}{\bar\rho}}u_\tau$. So we take $\sqrt{\frac{\bar\rho_w}{\bar\rho}}u_\tau$ to be the scale for W. In the inner and the outer layers of the boundary layer, W is assumed to be scaled as

$$\frac{W}{u_\tau}\sqrt{\frac{\bar\rho}{\bar\rho_w}} = f_{\text{inner}}(z^+), \tag{21}$$

$$\frac{W}{u_\tau}\sqrt{\frac{\bar\rho}{\bar\rho_w}} = f_{\text{outer}}(\eta), \tag{22}$$

where functions f_{inner} and f_{outer} are assumed to be independent of streamwise location x. The scaling of W above is not justified physically. However, W is very small relative to U and is not a dynamically dominant quantity. Thus, a rigorous treatment of W can be relaxed.

Applied at the recycling station and the inlet, the scaling of W leads to

$$(W)_i = \omega_{u_\tau}\omega_{\rho_w}\frac{(\bar\rho)_r}{(\bar\rho)_i}(W)_r, \tag{23}$$

for $(z^+)_r = (z^+)_i$ in the inner layer and $(\eta)_r = (\eta)_i$ in the outer layer. ω_{ρ_w} is given by

$$\omega_{\rho_w} = \frac{(\bar\rho_w)_i}{(\bar\rho_w)_r}. \tag{24}$$

Mean temperature

When fluctuations are small, to a first-order approximation, the mean temperature T and the mean density $\bar\rho$ are related by the state equation $T = \frac{P}{R\bar\rho}$ for perfect gas, where R is the gas constant. Thus, the rescaling of $\bar\rho$ follows once that of the mean temperature T is known.

The mean temperature appears in transformed mean streamwise velocities U^s, U^{**} and U^*. We need a relationship to decouple the mean streamwise velocity and the mean temperature and to produce the

rescaling of T in the process of rescaling U. For a zero-pressure-gradient boundary layer, Walz's equation is such a relation and is given by

$$\frac{T}{T_e} = \frac{T_w}{T_e} + \frac{T_r - T_w}{T_e}\left(\frac{U}{U_e}\right) - r\frac{\gamma-1}{2}M_e^2\left(\frac{U}{U_e}\right)^2, \quad (25)$$

where T_r is the recovery temperature, subscript e indicates a free stream quantity, M_e is the free stream Mach number, γ is the ratio of specific heats, and r it the recovery factor. The recovery temperature T_r and the recovery factor r are related by the definition of the recovery factor as

$$T_r = T_e\left(1 + r\frac{\gamma-1}{2}M_e^2\right). \quad (26)$$

For an adiabatic wall, $T_w = T_r$ and T_r is calculated by Eq. (26). For an isothermal wall, T_w is given and T_r is still calculated by Eq. (26). So Walz's equation tells us that the relation between the mean temperature and the mean streamwise velocity is dependent of the streamwise location only through T_r, or say the recovery factor r. If the streamwise distance from the recycling station to the inlet is not very large, it is a good assumption that r is the same at the recycling station and the inlet. So Walz's equation is also exactly the same at the two stations. We may generalize the argument by assuming that the relationship between the mean temperature and the mean streamwise velocity is independent of the streamwise location as long as the streamwise extent is not very large. For a boundary layer under non-zero pressure gradient, the relationship may not take the same form as Walz's equation, but its form is not needed as far as the rescaling method is concerned. We can obtain the relationship numerically at the recycling station and then use interpolation to decouple the mean streamwise velocity and the mean temperature at the inlet. To compute U^s and U^{**}, from which we obtain U and T, we start the integration from the wall, where the conditions are known. To compute U and T from U^*, we start the integration from the free stream, where the conditions also are known.

Turbulence rescaling

The scaling suggested by Morkovin to account for the mean-density variation appears appropriate to at least Mach 5. When the velocity fluctuations are normalized by the velocity scale $\sqrt{\frac{\bar{\rho}_w}{\bar{\rho}}}u_\tau$, they are in fair agreement with the incompressible data. Applied at the recycling station and the inlet, the scaling of u_i' ($i = 1, 2, 3$ corresponding to u',v',w') by $\sqrt{\frac{\bar{\rho}_w}{\bar{\rho}}}u_\tau$ leads to

$$(u_i')_i = \omega_{u_\tau}\omega_{\rho_w}\frac{(\bar{\rho})_r}{(\bar{\rho})_i}(u_i')_r, \quad (27)$$

for $(z^+)_r = (z^+)_i$ in the inner layer and $(\eta)_r = (\eta)_i$ in the outer layer. The difficulty is how to rescale the temperature, density and pressure fluctuations.

To a first-order approximation, the state equation yields

$$\frac{p'}{P} = \frac{T'}{T} + \frac{\rho'}{\bar{\rho}}. \quad (28)$$

In most cases, $\frac{p'}{P}$ is very small and can be assumed to be negligible, which gives

$$\frac{\rho'}{\bar{\rho}} = -\frac{T'}{T}. \quad (29)$$

Thus, only the temperature fluctuations need to be rescaled. The Strong Reynolds Analogy (SRA) serves to predict the relation between the temperature fluctuations and the streamwise velocity fluctuations and is given by

$$\frac{T_{\rm rms}}{T} = (\gamma-1)M_e^2\frac{u_{\rm rms}}{U}, \qquad R_{u'T'} = \frac{\overline{u'T'}}{u_{\rm rms}T_{\rm rms}} = -1, \quad (30)$$

where $T_{\rm rms}$ and $u_{\rm rms}$ are respectively the root mean squared temperature and velocity fluctuations. From the SRA, we can predict T' as

$$T' = -(\gamma-1)M_e^2\frac{u'}{U}T. \quad (31)$$

The problem is that the SRA is not well supported by simulation data even at low Mach numbers, see Refs. 1,27. We can avoid the problem in the same way as we deal with the relationship between the mean temperature and the mean streamwise velocity. We assume the following relations which are more general than the SRA,

$$\frac{T_{\rm rms}}{T} = f_{\rm amp}\frac{u_{\rm rms}}{U}, \quad \frac{T'(t)}{T_{\rm rms}} = c\frac{u'(t+f_{\rm phase})}{u_{\rm rms}}, \quad (32)$$

where t denotes time, c is equal to $+1$ (or -1) where u' and T' are positively (or negatively) correlated, $f_{\rm amp}$ and $f_{\rm phase}$ are functions of z^+ in the inner layer and η in the outer layer, and they are not functions of the streamwise location. Applying Eq. (32) to the recycling station and the inlet, we can deduce

$$\begin{aligned}(T'(t))_i &= \frac{(u'(t+f_{\rm phase}))_i}{(u'(t+f_{\rm phase}))_r}\frac{(U)_r}{(U)_i}\frac{(T)_i}{(T)_r}(T'(t))_r \\ &= \omega_{u_\tau}\omega_{\rho_w}\frac{(\bar{\rho})_r}{(\bar{\rho})_i}\frac{(U)_r}{(U)_i}\frac{(T)_i}{(T)_r}(T'(t))_r. \quad (33)\end{aligned}$$

Approaching the wall, $\frac{(U)_r}{(U)_i}$ becomes a $\frac{0}{0}$ type limit and can be evaluated according to L'Hospital rule. We thus have the following rescaling of the temperature fluctuations at the wall.

$$(T_w'(t))_i = \frac{\omega_{\rho_w}\omega_{\nu_w}}{\omega_{u_\tau}}\frac{(\bar{\rho})_r}{(\bar{\rho})_i}\frac{(T_w)_i}{(T_w)_r}(T_w'(t))_r. \quad (34)$$

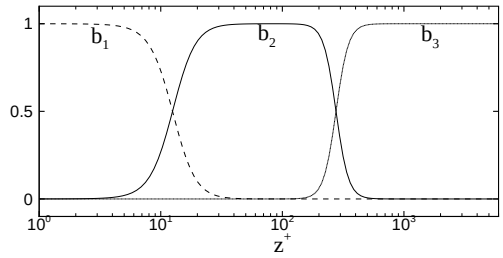

Fig. 5 The weight functions used in the simulation.

Rescaling parameters

To compute rescaling parameters $\omega's$, we need u_τ, ν_w, Δ (in our case, θ) and ρ_w at both the recycling station and the inlet. At the recycling station, these quantities are known. At the inlet, $(\nu_w)_i$ and $(\rho_w)_i$ can be found directly from the mean wall temperature $(T_w)_i$, θ can be specified and u_τ is given as a function of θ using Karman-Schoenherr equation under van Driest II transformation, see Ref. 31.

Implementation

In the rescaling of the mean streamwise velocity, three sublayers are distinguished. In the rescaling of other quantities, the boundary layer is divided into the inner sublayer and the outer sublayer. The composite profile of a quantity over the entire boundary layer is formed by a weighted combination of the profiles for all sublayers. For example, the streamwise velocity is formed as

$$u = \{U_{\rm visc} b_1(z) + U_{\rm log} b_2(z) + U_{\rm wake} b_3(z)\} + \{u'_{\rm inner}[1 - b_3(z)] + u'_{\rm outer} b_3(z)\}, \quad (35)$$

where $U_{\rm visc}$, $U_{\rm log}$ and $U_{\rm wake}$ represent the mean profiles in the viscous sublayer, the logarithmic region and the wake region respectively, $u'_{\rm inner}$ and $u'_{\rm outer}$ in turn represent the fluctuation profiles in the inner layer and the outer layer, and $b_1(z)$, $b_2(z)$ and $b_3(z)$ are weight functions. The weight functions are constructed from hyper-tangent functions as

$$b_1(k) = \frac{1}{2}\left\{1 - \tanh\left[c_1 \frac{k - k_{m1}}{k_{\rm logs} - k_{\rm visc}}\right]\right\}, \quad (36)$$

$$b_2(k) = \frac{1}{2}\left\{\tanh\left[c_1 \frac{k - k_{m1}}{k_{\rm logs} - k_{\rm visc}}\right] - \tanh\left[c_{23} \frac{k - k_{m23}}{k_{\rm wake} - k_{\rm loge}}\right]\right\}, \quad (37)$$

$$b_3(k) = \frac{1}{2}\left\{1 + \tanh\left[c_{23} \frac{k - k_{m23}}{k_{\rm wake} - k_{\rm loge}}\right]\right\}, \quad (38)$$

where k is the wall-normal grid index and equivalent to coordinate z, c_1 and c_{23} are constants to adjust the steepness of the weight functions, $k_{\rm visc}$, $k_{\rm logs}$, $k_{\rm loge}$ and $k_{\rm wake}$ are the wall-normal indices to distinguish different sublayers, $k_{m1} = \frac{k_{\rm visc}+k_{\rm logs}}{2}$ and $k_{m23} = \frac{k_{\rm loge}+k_{\rm wake}}{2}$. In the simulation presented in the next section, we choose $k_{\rm visc}$, $k_{\rm logs}$, $k_{\rm loge}$ and $k_{\rm wake}$ to correspond to $z^+ = 5$, $z^+ = 30$, $\frac{z}{\delta} = 0.2$ and $\frac{z}{\delta} = 0.5$ respectively. Fig. 5 shows the weight functions we used in the simulation.

In the mean scaling, a time average is needed to exclude the starting transient if the flow is initialized with a crude guess. In that case, the following formula is used.

$$U^{(m+1)} = w_1 U^{(m)} + w_2 \langle u^{(m+1)} \rangle_y, \quad (39)$$

where $U^{(m+1)}$ and $U^{(m)}$ are the time-averaged mean at time step $m+1$ and m respectively, $\langle u^{(m+1)} \rangle_y$ is the average of u in the spanwise direction at time step $m+1$, w_1 and w_2 are two weights satisfying $w_1 > 0, w_2 > 0, w_1 \gg w_2$ and $w_1 + w_2 = 1$. Lund *et al.*[2] let w_1 be $1 - \frac{\Delta t}{\tau}$ and w_2 be $\frac{\Delta t}{\tau}$, where Δt is the computational time step and τ the characteristic time scale of the averaging interval. From formula (39), we know

$$U^{(m+1)} = w_1^{m+1} U^{(0)} + w_2(w_1^m \langle u^{(1)} \rangle_y + w_1^{m-1} \langle u^{(2)} \rangle_y + \cdots + \langle u^{(m+1)} \rangle_y). \quad (40)$$

At the beginning of the simulation, because m is small and $w_1 \gg w_2$, $U^{(0)}$ takes a very large fraction of $U^{(m+1)}$, as seen from Eq. (40). Thus, we provide a smooth mean profile from TDNS as $U^{(0)}$ instead of using $\langle u^{(0)} \rangle_y$. We choose w_1 so that when the mean information has propagated from the inlet to the recycling station, m is large enough for $U^{(0)}$ to take almost no effect in $U^{(m+1)}$. After the transient, we increase w_1 to run for N steps in order to stabilize the statistics and then switch to a usual running average, i.e. $w_1 = 1 - \frac{1}{N+m-m_0}$ and $w_2 = \frac{1}{N+m-m_0}$, where m_0 is the step at which the running average begins. If $U^{(0)}$ is very crude and w_1 is not well attuned, the temporal starting transient can be very long before the right spatial behavior builds up over the boundary layer. If w_1 is too small, a good mean profile $U^{(m+1)}$ can not be achieved due to insufficiency of effective samples for averaging, which leads to wrong scaling and thus wrong boundary layer mean behavior.

If the initial flow field is crude, the rescaling parameters u_τ and θ that are specified at the inlet can largely differ from those calculated at the recycling station initially. The mean streamwise velocity rescaled by the law-of-the-wall thus has a large shift from the one rescaled by the-law-of-the-wake. When the mean profile of the streamwise velocity is formed by the weight functions, there appears an undershoot or overshoot in the profile. We call the start of a simulation with the undershoot or overshoot a jump start. It takes a long time to smooth the undershoot or overshoot and build up the right mean behavior over the whole boundary layer. A trick to avoid this is to let the initial u_τ and θ at the recycling station be the same as those specified at the inlet, and then use the averaging formula (39) to

initial flow conditions	M_e	$T_e[K]$	$\rho_e[kg/m^3]$	$10^3\delta_0[m]$	$10^3\delta_0^*[m]$	$10^4\theta_0[m]$
	4	5000	0.5	6.96	2.87	3.94
	Re_{θ_0}	$u_{\tau 0}[m/s]$	10^3C_{f0}			
	11363	243	0.96			
numerical set-up	L_x	L_y	L_z	N_x	N_y	N_z
	$6.10\delta_0$	$1.52\delta_0$	$10.30\delta_0$	384	128	128
	Δx^+	Δy^+	Δz^+	d_{station}		
	12.7	9.5	0.11-535	$2L_x$		

Table 1 Parameters for TDNS and ETDNS. $Re_{\theta_0} = \frac{\rho_e U_e \theta_0}{\mu_e}$. d_{station} **is the distance between two neighboring stations in ETDNS. Other symbols take their usual meaning.**

bring their right values at the recycling station slowly in the temporal transient of the simulation. In this way, the simulation starts smoothly. After the initial transient, the averaging formula (39) is discarded and u_τ and θ at the recycling station are calculated directly from the mean profile.

Tests

In this section, we simulate a supersonic turbulent boundary layer under zero pressure gradient. The perfect gas assumption is used and the specific heats, c_p and c_v, are assumed constants. The dynamic viscosity μ is assumed to obey a power law. We first present the comparisons between TDNS and ETDNS. We check the conditions for the validity of TDNS and point out the improvement over TDNS by ETDNS. We then present the results of a spatial DNS (SDNS) in which the rescaling method is implemented. The numerical results are compared with theoretical ones and those from the marching process of ETDNS. Scaling laws are verified by both SDNS and ETDNS.

We run ETDNS until a stationary station is reached and then take the final flow field as the initial conditions to run TDNS and ETDNS. Therefore, the initial flow parameters and numerical set-up are exactly the same for TDNS and ETDNS. These are given in Table 1. To save run time, a coarse spanwise mesh is used for comparisons below. The initial flow field for SDNS is from a quasi-stationary TDNS with a fine spanwise mesh. The initial flow parameters and numerical set-up of SDNS is given in Table 2. To compare results between SDNS and marching ETDNS, we also run ETDNS using the same initial flow field as SDNS. Thus, the marching ETDNS also has the fine mesh in the spanwise direction. We emphasize that all results in comparsions between TDNS and ETDNS are obtained with the coarse spanwise mesh and all results from the rescaling method are obtained with the fine spanwise mesh. For the resolution and domain assessments, we refer to Ref. 26.

The codes of TDNS, ETDNS and SDNS are essentially the same and are described in details in Ref.26. They use third-order shock-capturing weighted essentially non-oscillatory (WENO)schemes for the inviscid fluxes, fourth-order central-finite-difference schemes for viscous fluxes and a second-order accurate data-parallel lower-upper (DPLU) relaxation method for the time advancement. The ETDNS code has the extra forcing terms, which are treated explicitly. The marching scheme in ETDNS to approximate derivatives on the slow streamwise scale is a second-order backward finite difference scheme. No-slip and no-penetration conditions for velocity and an adiabatic condition for temperature are used at the lower wall. Symmetric boundary conditions are used at the top domain boundary. In SDNS, we generate the inflow using the rescaling method. The location of the recycling station is given in Table 2. We treat the outflow by placing a sponge layer[4,5] before the outflow boundary and applying symmetric boundary conditions at the outflow boundary. In the sponge layer, a vector quantity $\vec{Z} = -\sigma(x)(\vec{U} - \vec{U_0})$ is added to the right-hand side of the governing equations, where $\vec{U}$ stands for the vector of conservative variables and $\vec{U_0}$ a given steady basic flow. Because the recycling station is close to the sponge layer, we let $\vec{U_0}$ be the mean flow at the recycling station to reduce the artificial effects from the outflow treatment on the recycling station. Following Israeli *et al*,[32] the Newtonian cooling function $\sigma(x)$ is chosen to be

$$\sigma(x) = \mathcal{A}(\mathcal{N}+1)(\mathcal{N}+2)\frac{(x-x_s)^{\mathcal{N}}(L_x-x)}{(L_x-x_s)^{\mathcal{N}+2}}, \quad (41)$$

where $\mathcal{A}$ and $\mathcal{N}$ are two adjustable parameters chosen to be 4 and 3 respectively, x_s is the streamwise location where the sponge layer starts given in Table 2, and L_x is the streamwise length of the computational domain.

Comparisons between TDNS and ETDNS

Mean behavior

Fig. 6 shows the time history of friction velocity (averaged at the wall) and integral thickness in TDNS and ETDNS. In TDNS, the evolution of the skin friction is slow and its trend is not obvious in Fig. 6, but we may expect its decrease as the simulation goes much longer. The boundary layer thickening with time in TDNS indicates that the use of genuine periodic boundary conditions does lead to the temporal behavior of the

initial flow conditions	M_e	$T_e[K]$	$\rho_e[kg/m^3]$	$10^3\delta_0[m]$	$10^3\delta_0^*[m]$	$10^4\theta_0[m]$
	4	5000	0.5	7.44	3.28	4.11
	Re_{θ_0}	$u_{\tau 0}[m/s]$	$10^3 C_{f0}$			
	11742	255	1.01			
numerical set-up	L_x	L_y	L_z	N_x	N_y	N_z
	$5.71\delta_0$	$1.43\delta_0$	$9.64\delta_0$	384	256	128
	Δx^+	Δy^+	Δz^+	x_r	x_s	
	12.7	4.8	0.12-565	$4.6\delta_0$	$5.0\delta_0$	

Table 2 Parameters for SDNS. x_r is the streamwise location of the recycling station. x_s is the streamwise location where the sponge layer starts.

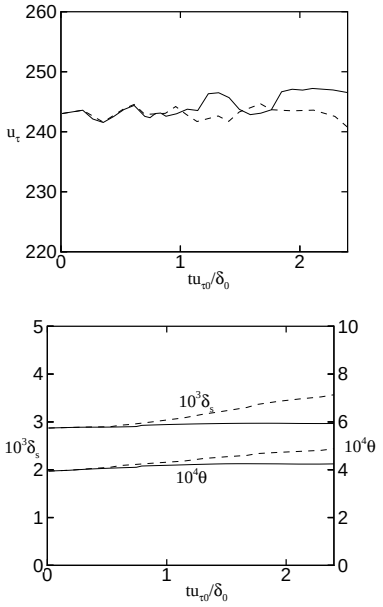

Fig. 6 The temporal evolution of the friction velocity and the integral thickness for TDNS and ETDNS. solid line: ETDNS, dashed line: TDNS.

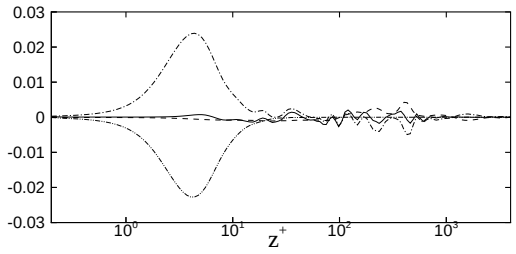

Fig. 7 The mean streamwise momentum balance in ETDNS. solid line: $\frac{\partial\langle\rho u\rangle}{\partial t}$, dashed line: $\langle f_u\rangle$, dash-dot line: $-\frac{\partial\langle\rho uw\rangle}{\partial z}$, dashdotdot line: $\frac{\partial\langle\tau_{xz}\rangle}{\partial z}$.

mean flow. In ETDNS, as expected, this temporal evolution is prohibited by the forcing, and the skin friction and the integral thickness evolve little with time.

If we estimate the time scale of the boundary layer growth as

$$t_g = \left(\frac{1}{\delta^*}\frac{\mathrm{d}\delta^*}{\mathrm{d}t}\right)^{-1}, \tag{42}$$

it is about $25\left(\frac{\delta_0^*}{u_{\tau 0}}\right)$ in TDNS for the duration shown in Fig. 6, where δ_0^* and $u_{\tau 0}$ are defined in the caption of Table 1. The total sampling time for the purpose of gathering statistics in TDNS is about $3\left(\frac{\delta_0^*}{u_{\tau 0}}\right)$, which is about one order of magnitude lower than the growth time. The boundary layer in TDNS can be considered quasi-steady if the flow adjusts to its local conditions much faster than the boundary layer growth. The adjusting time is of the order of the large-eddy-turn-over time $\frac{\delta_0}{U_e}$ and much smaller than the growth time. Thus, the conditions for the validity of TDNS are satisfied in the present simulation. Further comparisons between TDNS and ETDNS also validate the use of TDNS.

In ETDNS, the mean streamwise momentum balance is

$$\frac{\partial\langle\rho u\rangle}{\partial t} = -\frac{\partial\langle\rho uw\rangle}{\partial z} + \frac{\partial\langle\tau_{xz}\rangle}{\partial z} + \langle f_u\rangle, \tag{43}$$

where the terms at the right hand side represent advection, diffusion and forcing. Fig. 7 shows these terms normalized with the free stream momentum $\rho_e U_e$ and the large-eddy turn-over time $\frac{\delta}{U_e}$. From Fig. 7 we see that the time derivative of the mean streamwise momentum remains small in the boundary layer, with a maximum magnitude of less than 0.5%. Fig. 7 also shows that the advection and diffusion are dominant in the viscous sublayer and they nearly balance each other. Outside the viscous sublayer, the diffusion is very small, in turn the forcing and advection terms balance each other.

The profiles of the mean streamwise velocity and the mean temperature are compared in Fig. 8(a). A mean quantity here is obtained by averaging in both space and time. The difference between TDNS and ETDNS is small for each of these quantities. Fig. 8(b) plots the mean temperature versus the mean streamwise velocity and compare the resulting profiles with the one by Walz's equation. It can be seen that Walz's equation predicts very well the relationship between the mean streamwise velocity and the mean temperature

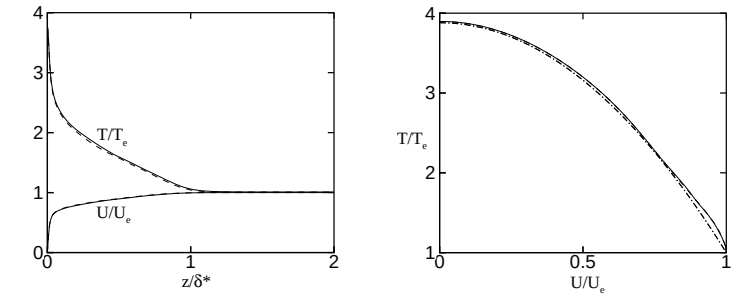

Fig. 8 The mean streamwise velocity and the mean temperature: (a) comparison between TDNS and ETDNS; (b) comparison with Walz's equation with $r = 0.9$. solid line: ETDNS, dashed line: TDNS, dashdot line: Walz's equation.

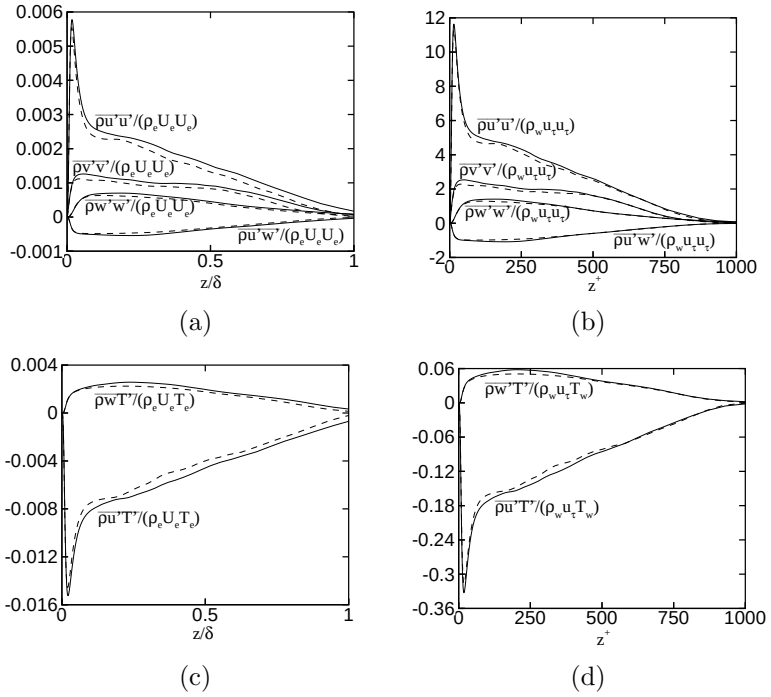

Fig. 9 Comparison between TDNS and ETDNS for (a) & (b) Reynolds stresses, (c) & (d) Reynolds heat fluxes. Quantities in (a) and (c) are nondimensionalized by the free stream parameters. Quantities in (b) and (d) are nondimensionalized by the wall parameters. solid line: ETDNS, dashed line: TDNS.

for the conditions chosen, and it can be used in the rescaling method for zero-pressure-gradient supersonic turbulent boundary layers.

Turbulence statistics

The Reynolds stresses and the Reynolds heat fluxes are compared between TDNS and ETDNS, as shown in Fig. 9. Primes are used to denote fluctuations with respect to the Reynolds-averaged mean. Due to the statistical symmetry in the spanwise direction, the Reynolds shear stresses $\overline{\rho u'v'}$ and $\overline{\rho v'w'}$ and the Reynolds heat flux $\overline{\rho v'T'}$ converge to zero, and they are not shown in Fig. 9. To observe the different temporal behavior of these quantities, we nondimensionalize them by the free stream parameters, i.e. ρ_e, U_e and T_e. As seen in Fig. 9, the magnitude of each Reynolds stress component in TDNS is less than the corresponding in ETDNS systematically. The reason for the systematical difference is that, in ETDNS, the flow can be statistically stationary , while in TDNS, the turbulence decays with time. Scaled with wall parameters, i.e. ρ_w, u_τ and T_τ ($T_\tau = T_w$ for an adiabatic wall and $T_\tau := \frac{P_{rw} q_w}{\rho_w C_{pw} u_\tau}$ for an isothermal wall, where P_{rw} is the Prandtl number and q_w the heat diffusion flux at the wall), we can still observe the similar difference for these quantities, which may indicate that the turbulence in TDNS evolves in a non-self-similar way. The same phenomena are also found for root mean squared fluctuating velocities, temperature and total temper-

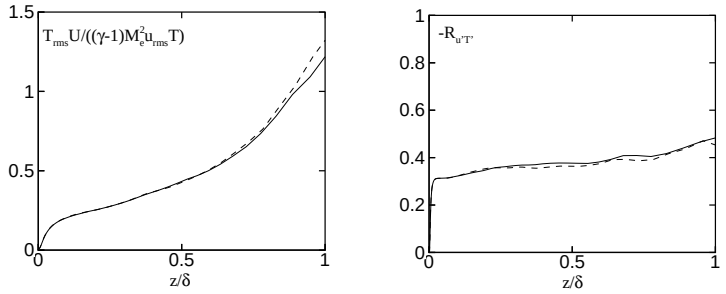

(a) (b)

Fig. 10 (a) Amplitude and (b) phase relationship between temperature fluctuations and streamwise velocity fluctuations. solid line: ETDNS, dashed line: TDNS.

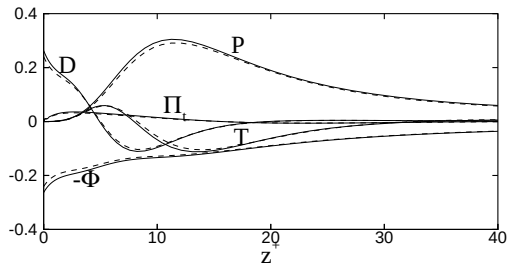

Fig. 11 The comparison of the TKE budget between TDNS and ETDNS. solid line: ETDNS, dashed line: TDNS.

ature. Nevertheless, the difference in the current and later comparisons between TDNS and ETDNS is very small, which means the use of TDNS is valid.

The SRA predicts the relation between the temperature fluctuations and the streamwise velocity fluctuations as in Eq. (30). From the SRA, we know $\frac{T_{rms}U}{(\gamma-1)M_e^2 T u_{rms}} = 1$ and $-R_{u'T'} = 1$. Fig. 10 plots $\frac{T_{rms}U}{(\gamma-1)M_e^2 T u_{rms}}$ and $-R_{u'T'}$ versus $\frac{z}{\delta}$ and indicates that the SRA is not satisfied in the bulk of the boundary layer simulated by both TDNS and ETDNS. In the rescaling method, we do not use the SRA.

After assuming homogeneity of turbulence in the streamwise and spanwise directions, the turbulent kinetic energy (TKE) budget equation reads

$$\frac{\partial}{\partial t}(\langle\rho\rangle\tilde{k}) + \tilde{w}\frac{\partial}{\partial z}(\langle\rho\rangle\tilde{k}) = \mathcal{P} + \mathcal{T} + \Pi_t + \Pi_d + \mathcal{D} - \Phi + \mathcal{V}_c, \quad (44)$$

where a quantity with a tilde is a Favre-averaged mean. The terms in Eq. (44) follow the usual interpretations. Fig. 11 gives the comparison of the TKE budget nondimensionalized by wall parameters between TDNS and ETDNS. Again, the small systematical difference exists and the reason for the difference is the same as in Fig. 9.

SDNS

The rescaling method results in a spatial boundary layer. Fig. 12 shows the spatial evolution of the boundary layer displacement thickness δ^*, momentum thickness θ, friction velocity u_τ and friction coefficient C_f. The rescaling method builds up the spatial boundary layer from the initial periodic flow field after the temporal transient is passed. The solid circles represent the time-averaged spatial distributions of these quantities for the spatial boundary layer in equilibrium. As seen from Fig. 12, the specified inlet friction velocity is as about 8% larger than the mean friction velocity of the initial flow field while the momentum thickness is the same, which makes the described trick necessary to avoid a jump start.

Sivells & Payne formula[31] under van Driest II transformation reads

$$F_c C_f = \frac{0.088[\lg(F_x Re_x) - 2.3686]}{[\lg(F_x Re_x) - 1.5]^3}, \quad (45)$$

$$F_\theta Re_\theta = \frac{0.044 F_x Re_x}{[\lg(F_x Re_x) - 1.5]^2}, \quad (46)$$

where C_f is the local skin friction coefficient, Re_x ($= \frac{\rho_e U_e x}{\mu_e}$) is Reynolds number based on distance to the virtual origin of the boundary layer, Re_θ is Reynolds number based on the momentum thickness as defined in Table 1. For a given Re_θ, we compute C_f from the estimation by Karman-Schoenherr equation under van Driest II transformation.[31] After C_f is calculated, we then compute Re_x from Eq. (45). Karman-Schoenherr equation under van Driest II transformation reads

$$\frac{1}{F_c C_f} = 17.08[\lg(F_\theta Re_\theta)]^2 + 25.11\lg(F_\theta Re_\theta) + 6.012. \quad (47)$$

F_c, F_θ and F_x are van Driest II transformation functions computed as

$$F_c = \frac{0.2 r M_e^2}{(\sin^{-1}\alpha + \sin^{-1}\beta)^2}, \quad (48)$$

$$F_\theta = \frac{\mu_e}{\mu_w}, \quad (49)$$

$$F_x = \frac{F_\theta}{F_c}, \quad (50)$$

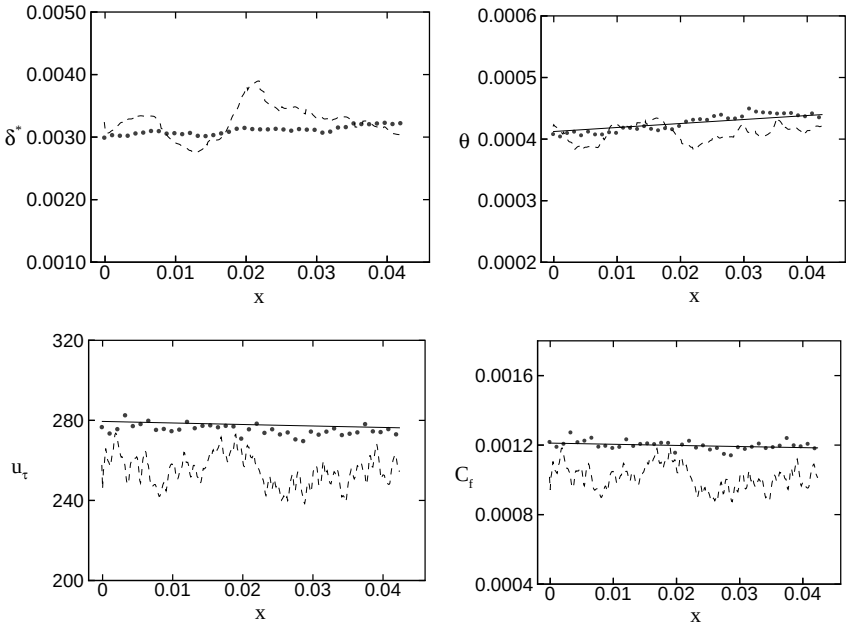

Fig. 12 Distributions of the displacement thickness δ^*, momentum thickness θ, friction velocity u_τ and friction coefficient C_f along the streamwise (x) direction. solid circles: SDNS, dashed lines: initial periodic flow field, solid lines: formulas from Least Square (LS) minimization.

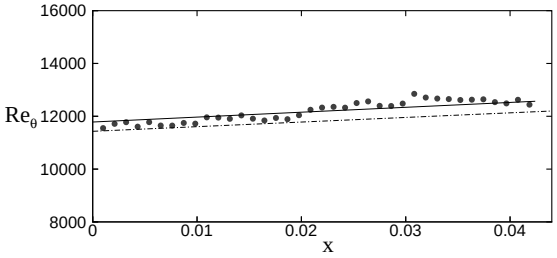

Fig. 13 Distribution of Re_θ along the streamwise (x) direction. solid circles: SDNS, dashdotted line: estimation by Eq. (45) and Eq. (47), solid line: formula from Least Square (LS) minimization.

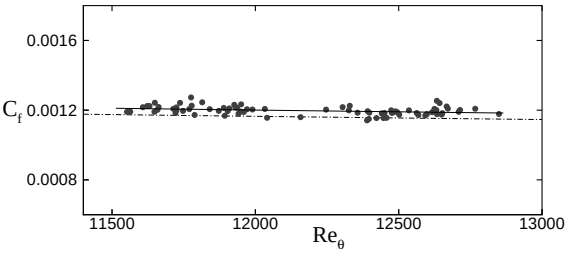

Fig. 14 Distribution of the local skin friction C_f in terms of Re_θ. Solid circles: SDNS, dashdotted line: Eq. (47), solid line: formula from LS minimization.

where r is recovery factor and α and β are calculated by

$$\alpha = \frac{2A^2 - B}{\sqrt{4A^2 + B^2}}, \tag{51}$$

$$\beta = \frac{B}{\sqrt{4A^2 + B^2}}, \tag{52}$$

with

$$A = \sqrt{\frac{0.2rM_e^2}{F}}, \tag{53}$$

$$B = \frac{1 + 0.2rM_e^2 - F}{F}, \tag{54}$$

$$F = \frac{T_w}{T_e}. \tag{55}$$

Fig. 13 shows that the streamwise evolution of Re_θ from the simulation is in excellent agreement with the one estimated by Eq. (45) and Eq. (47). Knowing u_τ, we calculate Re_x at the inlet from Eq. (45) and obtain data correspondence in SDNS between Re_θ and Re_x. We then use Least Square (LS) minimization to produce a formula similar to Eq. (46). The solid line in Fig. 13 represents the plot from the LS minimization. Its slope matches very well the slope estimated by Eq. (46). For comparison, we have shifted the virtual origin of the boundary layer to the boundary layer inlet. The relative magnitude difference between the LS results and the predictions by Eq. (46) is less than 2%. In Fig. 12, the LS results for θ distribution are given by a solid line.

Fig. 14 compares the simulated local skin friction C_f in terms of Re_θ with the estimation by Eq. (47). The dashdotted line is plotted from the estimation, solid circles denote time-averaged values from the spatial simulation. The solid line represents the results

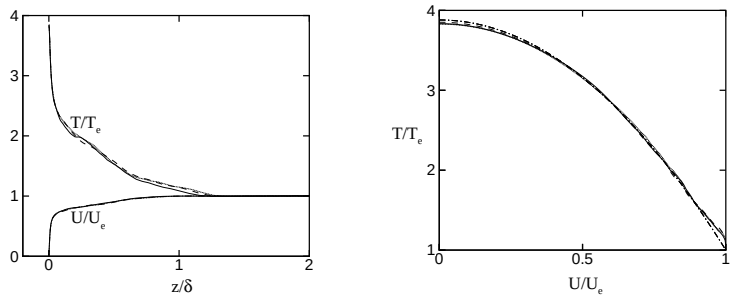

Fig. 15 The mean streamwise velocity and the mean temperature: (a) distributions, (b) comparison with Walz's equation with $r = 0.9$. dotted lines: station (1), dashed lines: station (2), solid lines: station (3), dashdot line: Walz's equation.

of the LS minimization which uses SDNS data to produce a formula similar to Eq. (47). As indicated by the comparison, the result from the simulation is in good agreement with the estimation. The relative magnitude difference between the LS results and the predictions by Eq. (47) is about 3.3%.

Fig. 15 (a) shows the mean streamwise velocity and the mean temperature, scaled by the free stream parameters, at three different streamwise stations marked as (1), (2) and (3) in Fig. 4 which respectively correspond to $x_1 = 0.3\delta_0$, $x_2 = 2.4\delta_0$ and $x_3 = 4.5\delta_0$. Because the evolution of the mean flow is very small due to the small streamwise extent, little difference is observed. Fig. 15 (b) plots the relationship between the mean streamwise velocity and the mean temperature at these stations. It can be seen that the relationship is independent of streamwise locations, which verifies the assumption we made in the rescaling method. For this zero-pressure-gradient boundary layer, Walz's equation can describe the relationship very well.

Fig. 16 (a) shows the mean streamwise velocity profiles under the transformation given by Eq. (9) at the three stations. The transformed velocity is scaled by u_τ, and the wall-normal coordinate is nondimensionalized by the wall units. Fig. 16 (a) indicates that the profiles are collapsed very well by the transformation and scaling in the viscous region ($z+ < 5$), and they satisfy the theoretical linear relationship in the viscous region very well. Fig. 16 (b) shows the van Driest transformed mean streamwise velocity profiles scaled with u_τ at the three stations. Results from TDNS and ETDNS are also included. The wall-normal coordinate is also nondimensionalized by the wall units. Fig. 16 (b) indicates that the profiles are collapsed very well by the transformation and scaling in the logarithmic region ($30 < z^+ < 200$ in our case), and they satisfy the theoretical logarithmic law in the logarithmic region very well. Near the boundary edge, the mean streamwise velocity profiles from SDNS, TDNS and ETDNS are not collapsed by the above manners, but as seen in

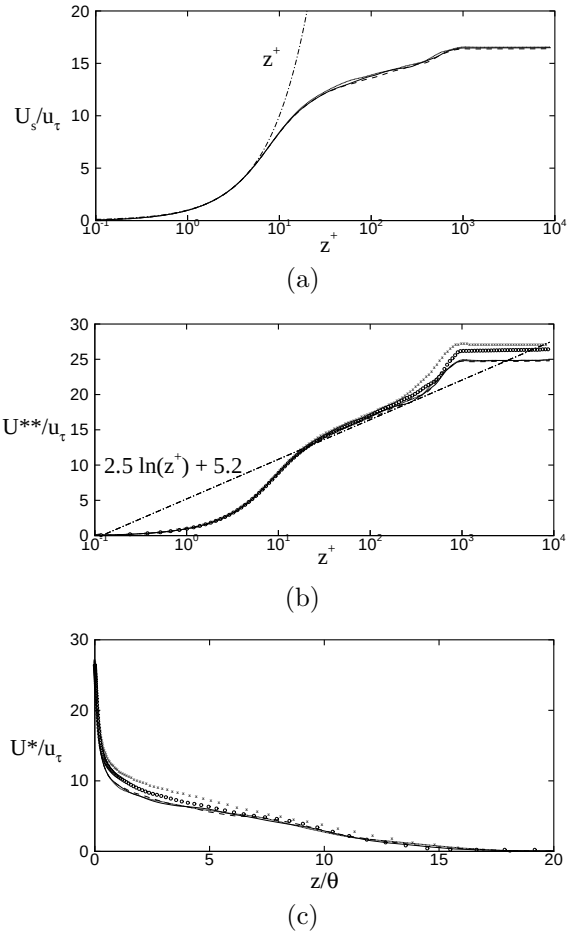

Fig. 16 Mean streamwise velocity (a) transformation by Eq. (9), (b) transformation by Eq. (15) and (c) transformation by Eq. (19). dotted lines: station (1), dashed lines: station (2), solid lines: station (3), x-mark: TDNS station, open circles: the fourth station of ETDNS.

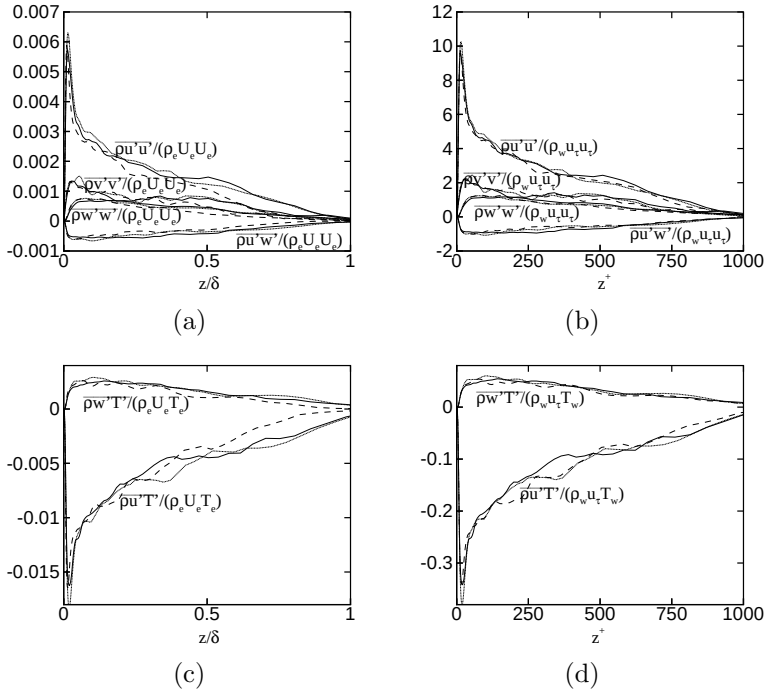

Fig. 17 The comparisons among stations (1), (2) and (3) for (a) & (b) Reynolds stresses, (c) & (d) Reynolds heat fluxes. Quantities in (a) and (c) are nondimensionalized by the free stream parameters. Quantities in (b) and (d) are nondimensionalized by the wall parameters. dotted lines: station (1), dashed lines: station (2), solid lines: station (3).

Fig. 16 (c), they are collapsed by the transformation given by Eq. (19) with the wall coordinate scaled by the momentum thickness. The transformation given by Eq. (19) is actually the van Direst transformation on the mean streamwise velocity defect.

Fig. 17 shows the profiles of Reynolds stresses and Reynolds heat fluxes at the three stations. They are obtained by averaging scaled Reynolds stresses and Reynolds heat fluxes in time. The wiggles on the profiles are due to the insufficiency of averaging samples. In Fig. 17 (a) and (c), the free stream parameters are used in scaling, and in Fig. 17 (b) and (d), the wall parameters are used. We may expect the spatial evolution of a Reynolds stress or a Reynolds heat flux from Station (1) to Station (3) is small because the three stations are close. While in Fig. 17 (a) and (c), the difference among the three stations is quite apparent. It may originate from the insufficiency of averaging samples. When scaled by wall parameters, the difference becomes much smaller, as indicated by Fig. 17 (b) and (d).

Fig. 18 plots $\frac{T_{rms}U}{(\gamma-1)M_e^2 T u_{rms}}$ and $-R_{u'T'}$ versus $\frac{z}{\delta}$ at the three stations. As seen from Fig. 18, it is a good assumption that the relationships between temperature fluctuations and streamwise velocity fluctuations are independent of the streamwise location, as expressed in Eq. (32), the rigorous SRA is not satisfied in the bulk of the boundary layer though.

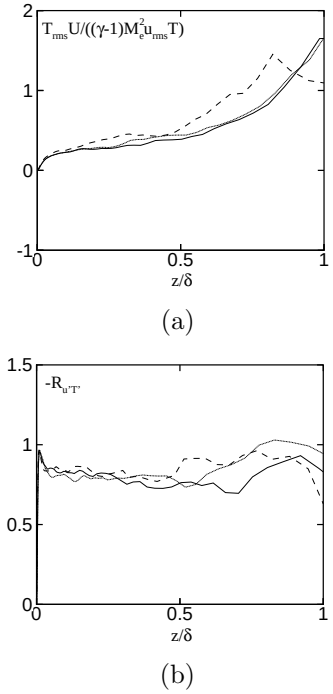

Fig. 18 Plots of the (a) amplitude and (b) phase relationships between the temperature fluctuations and the streamwise velocity fluctuations. dotted lines: station (1), dashed lines: station (2), solid lines: station (3).

Conclusions

Temporal simulations can be used to investigate a particular statistically stationary station of a turbulent boundary layer. The use of genuine periodic boundary conditions in a temporal simulation neglects the streamwise inhomogeneity of the boundary layer and thus results in evolving mean flow and decaying turbulence, but the usage is valid provided that the turbulence is quasi-steady and sustains for sufficient time to gather statistics without apparent boundary layer growth. The extended temporal approach adds forcing to the governing equations to account for the streamwise inhomogeneity and can achieve a statistically stationary mean flow and turbulence. The forcing is constructed from available information of flow evolution and no *a priori* assumptions about the flow are needed. The marching process in the extended approach allows simulations of a series of boundary layer stations.

The rescaling method proposed in this paper is designed for spatial simulation of a compressible turbulent boundary layer. The main assumptions behind the method are that the compressibility effects reduce to density variation effects and that general temperature-velocity relationships exist in the boundary layer. Based on similarity laws, the method rescales the flow field at a recycling station and then reintroduces the rescaled flow field to the inlet. The presented test indicates that the method results in a spatial simulation which generates its own inflow with little transient adjustment behind the inlet. The test is carried out over a zero-pressure-gradient flat plate, but the method may be extended to cases with pressure gradient and/or geometric change because the method does not assume any specific forms of similarity laws and temperature-velocity relationships. As pointed out by Lund *et al*[2] in their modified Spalart method, when the inlet is under a pressure distribution in equilibrium, the required changes in their method as well as ours involve only the computation of the friction velocity at the inlet and the vertical velocity distribution at the upper boundary.

Acknowledgments

This work was supported by the Air Force Office of Scientific Research under grant AF/F49620-02-1-0361 and the National Science Foundation under grant # CTS-0238390.

References

[1]Maeder, T., Adams, N., and Kleiser, L., "Direct simulation of turbulent supersonic boundary layers by an extended temporal approach," *J. Fluid Mech.*, Vol. 429, 2001, pp. 187–216.

[2]Lund, T., Wu, X., and Squires, K., "Generation of turbulent inflow data for spatially-developing boundary layer simulations," *J. Comput. Phys.*, Vol. 140, 1998, pp. 233–258.

[3]Streett, C. and Macaraeg, M., "Spectral multi-domain for large-scale fluid dynamic simulations," *Applied Numerical Mathematics*, Vol. 6, 1989, pp. 123–139.

[4]Guo, Y., Adams, N., and Kleiser, L., "A comparison study of an improved temporal DNS and spatial DNS of compressible boundary layer transition," *AIAA J.*, Vol. 34, 1996, pp. 683–690.

[5]Adams, N. A., "Direct numerical simulation of turbulent compression ramp flow," *Theoret. Comput. Fluid Dynamics*, Vol. 12, 1998, pp. 109–129.

[6]Spalart, P. and Watmuff, J., "Experimental and numerical study of a turbulent boundary layer with pressure gradients," *J. Fluid Mech.*, Vol. 249, 1993, pp. 337–371.

[7]Urbin, G. and Knight, D., "Large-Eddy Simulation of a Supersonic Boundary Layer Using an Unstructured Grid," *AIAA J.*, Vol. 39, No. 7, 2001, pp. 1288–1295.

[8]Spalart, P. and Yang, K., "Numerical study of ribbon-induced transition in Blasius flow," *J. Fluid Mech.*, Vol. 178, 1987, pp. 345–365.

[9]Spalart, P. R., "Direct simulation of a turbulent boundary layer up to $Re_\theta = 1410$," *J. Fluid Mech.*, Vol. 187, 1988, pp. 61–98.

[10]Li, N. and Piomelli, U., "Inflow conditions for large-eddy simulations of mixing layers," *Physics of Fluids*, Vol. 12, No. 4, 2000, pp. 935–938.

[11]Adams, N. A., "Direct simulation of the turbulent boundary layer along a compression ramp at $M = 3$ and $Re_\theta = 1685$," *J. Fluid Mech.*, Vol. 420, 2000, pp. 47–83.

[12]Rizzetta, D., Visbal, M., and Gaitonde, D., "Large-Eddy Simulation of Supersonic Compression-Ramp Flow by High-Order Method," *AIAA J.*, Vol. 39, No. 12, 2001, pp. 2283–2292.

[13]Rizzetta, D. and Visbal, M., "Application of Large-Eddy Simulation of Supersonic Compression Ramps," *AIAA J.*, Vol. 40, No. 8, 2002, pp. 1574–1581.

[14]Yao, Y., Thomas, T., Sandham, N., and Williams, J., "Direct numerical simulation of turbulent flow over a rectangular trailing edge," *Theoret. Comput. Fluid Dynamics*, Vol. 14, No. 5, 2001, pp. 337–358.

[15]Lee, S., Lele, S., and Moin, P., "Simulation of spatially evolving turbulence and the applicability of Taylor's hypothesis in compressible flow," *Phys. Fluids A*, Vol. 4, No. 7, 1992, pp. 1521–1530.

[16]Rai, M. and Moin, P., "Direct numerical simulation of transition and turbulence in a spatially evolving boundary layer," *J. Comput. Phys.*, Vol. 109, 1993, pp. 169–192.

[17]Le, H., Moin, P., and Kim, J., "Direct numerical simulation of turbulent flow over a backward-facing step," Tech. rep., Thermosciences Div., Dept. Mech. Engr., Stanford University, 1994, In Report TF-58.

[18]Klein, M., Sadiki, A., and Janicka, J., "A digital filter based generation of inflow data for spatially developing direct numerical or large eddy simulations," *J. Comput. Phys.*, Vol. 186, No. 2, 2003, pp. 652–665.

[19]Bhaganagar, K., Rempfer, D., and Lumley, J., "Direct Numerical Simulation of Spatial Transition to Turbulence using Fourth-Order Vertical Velocity Second-Order Vertical Vorticity Formulation," *J. Comput. Phys.*, Vol. 180, No. 1, 2002, pp. 200–228.

[20]Adams, N. A. and Kleiser, L., "Numerical Simulation of Transition in a Compressible Flat Plate Boundary Layer," *ASME: Transitional and Turbulent Compressible Flows*, 151, 1993, pp. 101–110.

[21]Fasel, H. and Konzelmann, U., "Non-parallel stability of a flat-plate boundary layer using the complete Navier-Stokes equations," *J. Fluid Mech.*, Vol. 221, 1990, pp. 311–347.

[22]Ducros, F., Comte, P., and Lesieur, M., "Large-eddy simulation of transition to turbulence in a boundary layer developing spatially over a flat plate," *J. Fluid Mech.*, Vol. 326, 1996, pp. 1–36.

[23]Pruett, C. and Chang, C., "Direct numerical simulation of hypersonic boundary-layer flow over a flared cone," *Theoret. Comput. Fluid Dynamics*, Vol. 11, 1998, pp. 49–67.

[24]Kleiser, L. and Zang, T., "Numerical simulation of transition in wall-bounded shear flows," *Annu. Rev. Fluid Mech.*, Vol. 23, 1991, pp. 495–537.

[25]Lin, C. C., "On Taylor's hypothesis and the acceleration terms in the Navier-Stokes equations," *Q. Appl. Math.*, Vol. 10, 1953, pp. 295.

[26]Martin, M. P., "DNS database of hypersonic turbulent boundary layers," *AIAA Paper No. 03-3726*, 2003.

[27]Guarini, S., Moser, R., Shariff, K., and Wray, A., "Direct numerical simulation of a supersonic turbulent boundary layer at Mach 2.5," *J. Fluid Mech.*, Vol. 414, 2000, pp. 1–33.

[28]Garnier, E., Sagant, P., and Deville, M., "Large Eddy Simulation Shock/Boundary-Layer Interaction," *AIAA J.*, Vol. 40, No. 10, 2002, pp. 311–347.

[29]Smits, A. and Dussauge, J., *Boundary Layer Mean-Flow Behavior*, AIP PRESS, 1996, In Turbulent Shear Layers in Supersonic Flows.

[30]Patel, V., "Calibration of the Preston tube and limitations on its use in pressure gradients," *J. Fluid Mech.*, Vol. 23, 1965, pp. 185–208.

[31]Hopkins, E. and Inouye, M., "An evaluation of theories for predicting turbulent skin friction and heat transfer on flat plates at supersonic and hypersonic Mach numbers," *AIAA J.*, Vol. 9, No. 6, 1971, pp. 993–1003.

[32]Israeli, M. and Orszag, S., "Approximation of Radiation Boundary Conditions," *J. Comput. Phys.*, Vol. 41, 1981, pp. 115–135.